Electrochemically induced amorphous-to-rock-salt phase transformation in niobium oxide electrode for Li-ion batteries

Pete Barnes [1,2], Yunxing Zuo[3], Kiev Dixon[1], Dewen Hou[1,4], Sungsik Lee[5], Zhiyuan Ma[5], Justin G. Connell [6], Hua Zhou [5], Changjian Deng[1], Kassiopeia Smith[1], Eric Gabriel[1], Yuzi Liu [4], Olivia O. Maryon[1], Paul H. Davis [1], Haoyu Zhu[1], Yingge Du [7], Ji Qi[3], Zhuoying Zhu[3], Chi Chen [3], Zihua Zhu [8], Yadong Zhou [8], Paul J. Simmonds [1,9], Ariel E. Briggs[1], Darin Schwartz[10], Shyue Ping Ong [3]✉ and Hui Xiong [1,11]✉

Intercalation-type metal oxides are promising negative electrode materials for safe rechargeable lithium-ion batteries due to the reduced risk of Li plating at low voltages. Nevertheless, their lower energy and power density along with cycling instability remain bottlenecks for their implementation, especially for fast-charging applications. Here, we report a nanostructured rock-salt Nb_2O_5 electrode formed through an amorphous-to-crystalline transformation during repeated electrochemical cycling with Li^+. This electrode can reversibly cycle three lithiums per Nb_2O_5, corresponding to a capacity of 269 mAh g⁻¹ at 20 mA g⁻¹, and retains a capacity of 191 mAh g⁻¹ at a high rate of 1 A g⁻¹. It exhibits superb cycling stability with a capacity of 225 mAh g⁻¹ at 200 mA g⁻¹ for 400 cycles, and a Coulombic efficiency of 99.93%. We attribute the enhanced performance to the cubic rock-salt framework, which promotes low-energy migration paths. Our work suggests that inducing crystallization of amorphous nanomaterials through electrochemical cycling is a promising avenue for creating unconventional high-performance metal oxide electrode materials.

ncreasing global energy demand has intensified the pursuit of high-performance, cost-effective and sustainable energy storage technologies[1]. While rechargeable lithium-ion batteries are the current market leader, innovative battery materials created with novel processing techniques are needed to reach new performance benchmarks. Niobium oxides are promising negative electrode materials for rechargeable lithium-ion batteries due to their rich redox chemistry (Nb^{5+} to Nb^{1+}), chemical stability, and numerous metastable and stable polymorphs[2–8]. The higher intercalation potential of Nb_2O_5 (~1.7 V versus Li/Li^+) relative to commercial graphite electrodes (<0.3 V) makes it less susceptible to Li plating and electrolyte decomposition, and therefore safer[8]. However, sluggish Li^+ diffusion, poor electrical conductivity (~3×10^{-6} S cm⁻¹)[5] and low capacity have hindered the deployment of Nb_2O_5 electrodes[8–10]. To address these issues, work has focused on increasing charge storage and transport properties by developing nanoarchitectures and/or adding conductive materials (for example, graphene and carbon coatings)[8,11–13].

Another strategy to improve the performance of Nb_2O_5 electrodes is to optimize the crystal structure for lithium ion intercalation. There are at least 12 different polymorphs of Nb_2O_5 (ref. [5]). Polymorphs of Nb_2O_5 previously studied as lithium-ion battery negative electrodes include pseudohexagonal (TT-Nb_2O_5),

orthorhombic (T-Nb_2O_5) and monoclinic (B-, M- and H-Nb_2O_5)[14,15]. The average capacity of the most studied T-Nb_2O_5 electrodes is around 170 mAh g⁻¹ (refs. [5,10,16]), while a higher capacity of 227 mAh g⁻¹ has been reported for a monoclinic structure[6], which is beyond the theoretical capacity of 202 mAh g⁻¹ based on $Li_2Nb_2O_5$, that is, one electron redox per Nb.

Currently, strategies for the synthesis of new intercalation metal oxide electrode materials include traditional ceramic processing by solid-state reactions, hydro(solvo)thermal processing and ionothermal processing. However, metastable structures with unique properties cannot be easily obtained through such approaches. Recent studies on other transition metal oxides have suggested that electrochemical cycling may present a new synthetic avenue to obtain novel structures and frameworks[17–21].

The first demonstration of this phenomenon in transition metal oxide negative electrodes was with titanium dioxide nanotubes (TiO_2NT)[18], wherein amorphous TiO_2NT underwent spontaneous phase transformation into a long-range-ordered/short-range-disordered cubic structure when cycled with Li^+ (ref. [18]). Studies showed that when Li^+ reached a high concentration, atomic rearrangements were initiated within the material to minimize the energy, resulting in a cubic structure[18,19]. Recently, a disordered rock-salt (DRX) $Li_{3+x}V_2O_5$ electrode obtained through
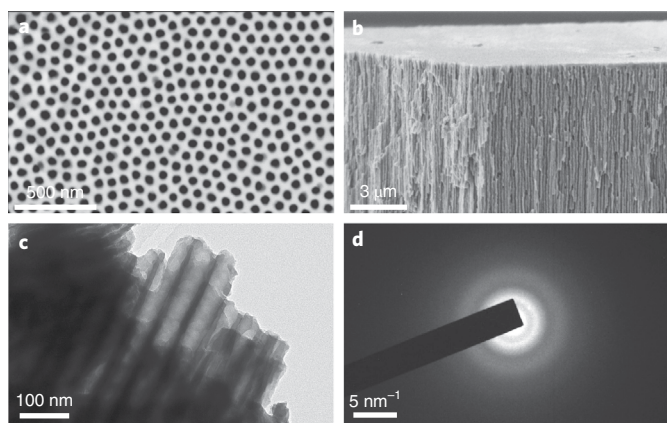
Fig. 1 | Characterization of the as-prepared NCNO. a,b, Top view (**a**) and side view (**b**) scanning electron microscopy (SEM) images of the as-prepared samples. The NCNO has uniform pores with ~56.3 ± 2.3 nm average pore diameter and ~28 ± 8 nm wall thickness. **c,d**, Low magnification TEM image (**c**) and SAED (**d**) of the as-prepared NCNO, where the diffuse ring indicates its amorphous nature.

electrochemically lithiating V_2O_5 to 1.5 V exhibited an exceptional rate capability for fast-charging lithium-ion batteries[21]. Furthermore, it was also shown in a manganese oxide system that a tunnel-structured todorokite, which is common in nature but difficult to synthesize in the laboratory at room temperature, can be obtained through repeated electrochemical cycling from a layered MnO_2 (ref. [20]).

Here, we report an electrochemically driven amorphous-to-crystalline (a-to-c) transformation of nanostructured Nb_2O_5 upon cycling with Li^+, and demonstrate the insertion of three lithiums into Nb_2O_5 (~1.5 electron redox per Nb). Amorphous Nb_2O_5 (a-Nb_2O_5) transformed spontaneously to a rock-salt structure (RS-Nb_2O_5) when the electrode was cycled to a potential of 0.5 V versus Li/Li^+, as identified by transmission electron microscopy (TEM) and synchrotron X-ray diffraction. Density functional theory (DFT) calculations revealed that RS-Nb_2O_5 exhibits an exceptionally high capacity for Li^+ storage and low migration barriers for Li^+ diffusion. Results from X-ray photoelectron spectroscopy (XPS) and X-ray absorption spectroscopy (XAS) indicated that the high capacity of RS-Nb_2O_5 was associated with its ability to go beyond the Nb^{5+}/Nb^{4+} redox. In addition, the RS structure benefited from an increase in Li^+ diffusivity and electrical conductivity compared to its amorphous counterpart, as shown by galvanostatic intermittent titration technique (GITT), peak force tunnelling atomic force microscopy (PF-TUNA) and two-point probe conductivity measurement, which correlated closely with its rate performance. Electrochemically induced crystallization of nanomaterials therefore offers an innovative approach for the discovery of high energy/power and stable electrode materials that were previously inaccessible using conventional synthesis methods.

Characterization of As-prepared nanochanneled Nb_2O_5

As-prepared samples consist of vertically oriented nanochanneled niobium oxide (NCNO) electrically connected to a Nb current collector (Fig. 1 and Supplementary Fig. 1). This particular nanoarchitecture facilitates fast access of the electrolyte to the active walls, as well as facile electron and ion transport for enhanced kinetics[22]. Selected area electron diffraction (SAED; Fig. 1d), X-ray diffraction and Raman spectroscopy (Supplementary Fig. 2) showed that the as-prepared NCNO was amorphous.

The a-to-c transformation of NCNO via electrochemical cycling

The as-prepared NCNO samples were subjected to electrochemical cycling between 3 V and 0.5 V versus Li/Li^+, and the voltage (V) profiles and corresponding differential capacity (dQ/dV) plots for the electrode are shown in Fig. 2. The voltage profile of the initial discharge is characterized by a shallow, linear slope, which upon subsequent cycling develops a plateau-like feature centred around 1.67 V (Fig. 2a). The appearance of a plateau is indicative of an increased number of equivalent intercalation sites in a crystalline host material representing a first-order phase transition during intercalation/deintercalation[23], which suggests an a-to-c phase transformation initiated by electrochemical cycling with Li^+.

Figure 2a exhibits a large hysteresis during the initial cycle, which may result from mechanical stress, thermodynamic entropic effects, activation polarization, nucleation barriers and/or lattice distortions within the active material[24–28]. A substantial reduction in the hysteresis was observed on the 5th and 20th cycles. This demonstrates that the electrode self-improved its thermodynamic and kinetic properties through repeated Li insertion/extraction.

The corresponding differential capacity analysis is shown in Fig. 2b, which allows in-depth identification of phase evolution and self-improvement within the material upon electrochemical cycling. The results highlight the a-to-c phase transformation occurring below 1.1 V (blue dashed box in Fig. 2b). In the first cycle, the electrode exhibited a capacitor-like response within the majority of the potential window, consistent with previous work by Kim et al.[7], with the exception of below 1.1 V during lithiation. In this region, a cathodic peak developed around 0.78 V and continued to appear on the initial three cycles, which is associated with the a-to-c phase transformation. The corresponding anodic peak appeared near 2.31 V. The large peak-to-peak separation is consistent with the large hysteresis seen in Fig. 2a, suggesting initially high nucleation barriers and sluggish kinetics in the intermediate phase, as sluggish charge transfer kinetics cause greater separation of the cathodic and anodic peaks (ΔE_p). By the fourth cycle, the redox peaks near 0.78 V and 2.3 V almost disappeared. Concurrently, a distinct redox peak pair started to evolve around 1.67 V, which suggests a new phase was formed. The ΔE_p decreased from 140 mV on the 5th cycle to 74 mV on the 100th cycle, indicating continued improvement of the newly formed phase (Supplementary Fig. 3). This observation also implies that the new Nb_2O_5 structure, formed upon a-to-c transformation electrochemically, offers improved charge storage and transport kinetics.

Structural characterization of a-to-c Nb_2O_5 electrode

TEM, grazing-incidence synchrotron X-ray diffraction and ex situ extended X-ray absorption fine structure (EXAFS) were conducted to elucidate the new rock-salt phase of Nb_2O_5 (Fig. 3). The phase transformation upon electrochemical cycling between 3 V and 0.5 V was first evaluated via SAED and high-resolution TEM (Fig. 3a–f). The pristine sample exhibited diffuse rings in SAED (Fig. 3a), consistent with the amorphous feature observed in high-resolution TEM (Fig. 3d). The SAED pattern began to sharpen after the first cycle (Fig. 3b), suggesting the formation of nanocrystallites within the amorphous matrix (Fig. 3e). After the 20th cycle, both SAED and high-resolution TEM showed that the oxide had become fully crystalline (Fig. 3c,f). In addition, focused ion beam - TEM and ex situ TEM were performed at different locations on an electrode after 100 cycles (Supplementary Figs. 4 and 5) as well as on electrodes at different states of charge (Supplementary Fig. 6). It was shown that the electrode remained crystalline, with no evidence of large amorphous regions or intermediates. Furthermore, grazing-incidence synchrotron X-ray diffraction of the delithiated sample (Supplementary Fig. 7) showed no notable change in peak shape or peak position at different incidence angles, that is,
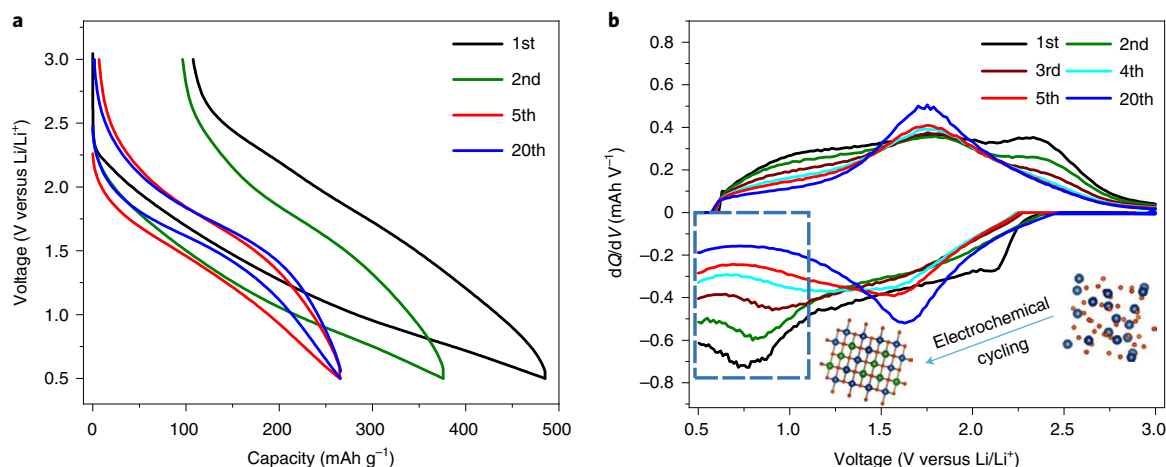
Fig. 2 | Voltage profiles and differential capacity plots of the NCNO subjected to electrochemical cycling. a, Voltage profiles of the NCNO electrode for the first 20 cycles. **b**, Differential capacity (dQ/dV) plots between 3 and 0.5 V versus Li/Li⁺. The peak below 1.1 V during discharge (lithiation) is evidence of the a-to-c transformation (blue dashed box). The disappearance of the cathodic peak below 1.1 V beyond the third cycle is the evidence that the phase transformation had nearly completed. The inset illustrates the amorphous Nb_2O_5 (right) to rock-salt $Li_3Nb_2O_5$ (left) phase transformation during electrochemical lithiation.

probing depths. Thus, the sample remains nanocrystalline throughout, indicating the uniformity of the film and insignificant surface disorders. This further suggests the new crystalline structure obtained through electrochemical cycling accounts for the performance improvement compared to its initial amorphous counterpart, which will be discussed later.

We determined the structure of the crystalline phase after the 20th cycle with ex situ grazing-incidence synchrotron X-ray diffraction (Fig. 3g). We indexed all major peaks to a (to the best of our knowledge) previously unreported Nb_2O_5 cubic rock-salt phase with the space group of $Fm\bar{3}m$. The lattice parameter a of the cubic structure is 4.146(7) Å. Based on the Scherrer equation[29], the new phase has a crystallite size of ~10 nm. To exclude the possibility that the charged (delithiated) electrode could be the rock-salt lithium niobate (Li_3NbO_4), additional results were obtained from the secondary-ion mass spectrometry depth profile (Supplementary Fig. 8) and inductively coupled plasma mass spectrometry. The results confirm that the new phase is RS-Nb_2O_5 and not RS-Li_3NbO_4 (Supplementary Information). Notably, the a-to-c phase transformation was not observed when the NCNO electrode was cycled above 1.1 V even with extended cycling, and the electrode remained amorphous (Supplementary Figs. 2a and 9).

Ex situ EXAFS analysis was used to examine the local structural evolution of Nb during the first discharge (lithiation; Fig. 3h). EXAFS spectra for Nb, NbO_2 and Nb_2O_5 standards are provided in Supplementary Fig. 10. In the pristine sample, two broad peaks near 1.6 Å and 2.5 Å were assigned to the Nb–O and Nb–Nb bonds[10], respectively. The amorphous material contains distorted NbO_6, NbO_7 and NbO_8, causing large variation in the Nb–O and Nb–Nb distances[4]. Discharging to lower voltages led to narrowing of the Nb–O peak, accompanied by an intensity increase in the Nb–Nb peak (Supplementary Table 1). This implies the a-to-c transformation. The a-to-c transformation would require ordering of the distorted polyhedra, leading to converging radial distances, and higher intensity from the coordinated Nb–O and Nb–Nb shell.

Multielectron redox of the RS-Nb_2O_5 electrode

Ex situ Nb K-edge X-ray absorption near edge structure (XANES) and XPS were carried out to evaluate the valence state of Nb in the sample at various states of discharge (Fig. 4a,b). The XANES spectrum from the pristine sample most closely matched the H–Nb_2O_5

standard, indicating a Nb oxidation state in the bulk of around +5. Upon discharging to 1 V, the edge position of the sample nearly matched the NbO_2 standard, suggesting the Nb oxidation state decreased to +4. A further discharge to 0.5 V shifted the edge of the spectrum to even lower energy, indicating a Nb oxidation state below +4 in the bulk of the electrode.

Ex situ Nb 3d core level XPS spectra (Fig. 4b) were obtained from electrodes at open-circuit voltage, discharged to 1.0 V and 0.5 V, and charged back to 3.0 V. At open circuit, the sample exhibited $Nb_{3/2}$ and $Nb_{5/2}$ peaks at 209.5 and 206.7 eV, indicating Nb^{5+} (refs. [30,31]). Upon discharging to 1 V, the primary peaks were shifted 1.0 eV lower, consistent with the reduction from Nb^{5+} to Nb^{4+} seen in the XANES spectra[32]. In addition, two new sets of doublets appeared at lower binding energies of 206.5/203.6 eV and 205.4/202.6 eV, corresponding to Nb^{2+} and Nb^{1+}, respectively[33,34]. Further discharging to 0.5 V resulted in increased intensity of the Nb^{1+} peak relative to the Nb^{2+} and Nb^{4+} peaks, suggesting significant reduction of Nb. As XPS is a surface technique (probing the top 10 nm of a surface)[35], the results suggest that the surface of the RS-Nb_2O_5 may experience larger reduction, forming suboxides not present in the bulk[36]. Upon charging back to 3.0 V, the electrode returned to Nb^{5+}, with only minimal residual Nb^{4+} and Nb^{2+}. The XPS results demonstrate that the Nb in RS-Nb_2O_5 undergoes multielectron redox in Nb (>1:1 Li/Nb) upon lithiation/delithiation and that the process is reversible. By comparison, a DRX Li_3NbO_4 has been reported as a high-capacity positive electrode, but it was claimed that the Nb ion stayed pentavalent throughout the charging/discharging processes and the charge compensation was achieved through solid-state redox of oxygen ions[37].

The voltage profile for lithium intercalation into RS-Nb_2O_5 was simulated using DFT. The pseudo-binary RS-Nb_2O_5-$Li_3Nb_2O_5$ phase diagram constructed from these calculations is shown in Fig. 4c, and the calculated and experimental voltage profiles are plotted in Fig. 4d. Overall, the average Perdew–Burke–Ernzerhof voltage is 1.76 V, which is in excellent agreement with the experimental average voltage of 1.67 V.

High rate performance and cycling stability

The rate capability of RS- and a-Nb_2O_5 electrodes at different current rates of 20, 50, 100, 200 and 1,000 mA g⁻¹ is shown in Fig. 5a. The RS-Nb_2O_5 electrode exhibited a high reversible capacity of
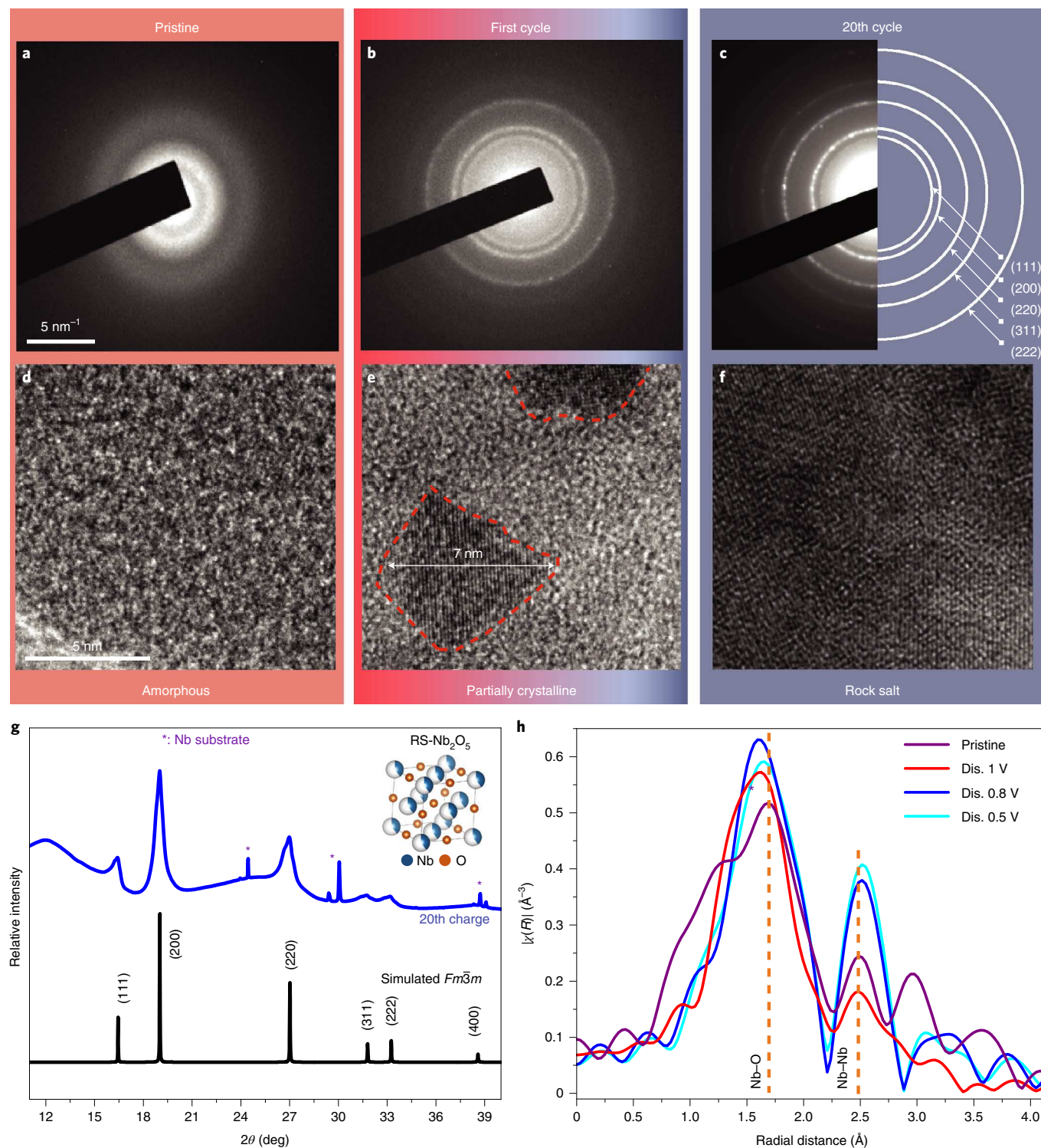
Fig. 3 | SAED and high-resolution TEM images of the NCNO samples at different stages of electrochemical cycling; grazing-incidence X-ray diffraction of a cycled NCNO sample; and Nb K-edge EXAFS of samples at different states of discharge. a–c, SAED images of samples in the pristine state, after the 1st cycle and after the 20th cycle, respectively. **d–f**, Corresponding high-resolution TEM images of the samples in **a–c**. For the pristine state, diffuse rings in SAED and an absence of periodic structures in high-resolution TEM demonstrate its amorphous nature. After the first cycle, faint and broadened diffraction rings appear in SAED. Defined grains are visible in high-resolution TEM, and a ~7 nm crystallite with a lattice spacing of 2.14 Å is seen, indicative of the corresponding (200) planes in the cubic rock-salt phase. After the 20th cycle, the phase becomes fully crystalline, displaying well-defined SAED rings and crystalline domains in high-resolution TEM. **g**, Grazing-incidence synchrotron X-ray diffraction of the NCNO electrode at the charged state (delithiated) after 20 cycles. The structure is in good agreement with the simulated rock-salt Nb_2O_5 phase (black, space group $Fm\bar{3}m$) with a lattice spacing of 4.146(7) Å. A unit cell of RS-Nb_2O_5 is presented in the inset. **h**, Fourier-transformed EXAFS spectra (not phase-shift corrected) at the Nb K edge of the NCNO electrodes during the first discharge (Dis.) at different voltages. The narrowing of the Nb–O peak and increasing intensity of the Nb–Nb peak upon discharging below 1 V reveal the process of a-to-c transformation. $\chi(R)$ is the Fourier-transformed, normalized, background subtracted fine-structure component of the EXAFS spectrum. R is the radial distance.
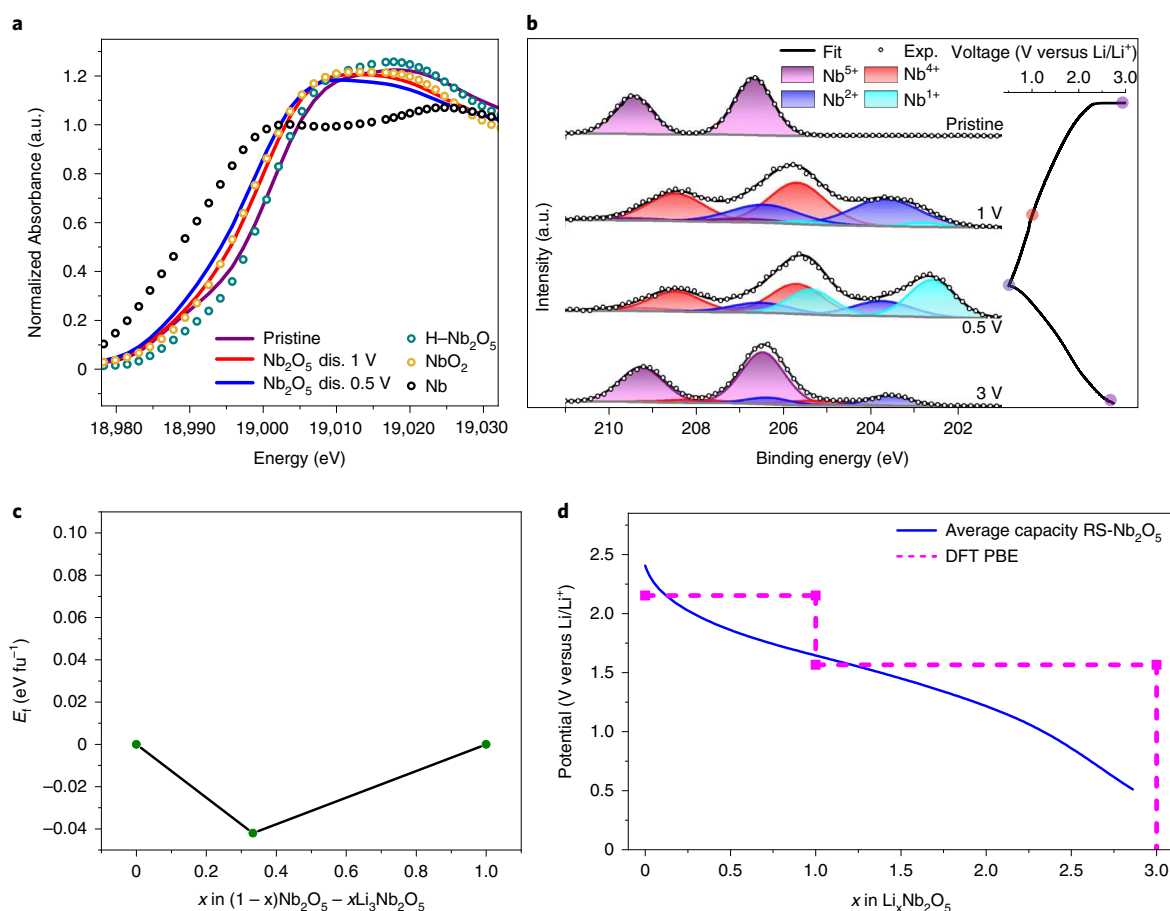
Fig. 4 | Characterization of the oxidation state of Nb in RS-Nb$_2$O$_5$; compound phase diagram computed by Perdew–Burke–Ernzerhof; and voltage profiles of Li$_x$Nb$_2$O$_5$. a, Nb K-edge XANES of Nb$_2$O$_5$ electrodes at various states of discharge. The lower edge position of the electrode discharged at 0.5 V compared to the standard NbO$_2$ indicates an oxidation state of Nb lower than +4. **b**, XPS spectra of the RS-Nb$_2$O$_5$ electrodes upon lithiation/delithiation processes in the range 3–0.5 V. The corresponding voltage profile is shown on the right. The potentials of the ex situ samples are marked by colored circles. Exp., experiment. **c**, The compound phase diagram of the formation energy (E_f) per formula unit (fu) against composition was computed using the Perdew–Burke–Ernzerhof (PBE) functional. The two end members are Nb$_2$O$_5$ and Li$_3$Nb$_2$O$_5$. The compositional resolution of $x = 0.5$ increments in Li$_x$Nb$_2$O$_5$. An intermediate stable phase was observed at the composition LiNb$_2$O$_5$. **d**, Comparison between experimental and computed voltage profiles of Li$_x$Nb$_2$O$_5$ ($0 \leq x \leq 3$) upon electrochemical cycling. The average Perdew–Burke–Ernzerhof voltage of 1.76 V agrees with the measured voltage of 1.67 V.

269 mAh g^{-1} at a current density of 20 mA g^{-1}, corresponding to ~1.42 electron redox per Nb. The high capacity of RS-Nb$_2$O$_5$ is among the best of reported values for Nb$_2$O$_5$ and niobate electrodes (Supplementary Fig. 11)[6,16,38,39]. Additionally, we observed a <10% drop in capacity at an increased current rate of 200 mA g^{-1} (243 mAh g^{-1}), while at a current rate of 1,000 mA g^{-1} the electrode capacity was slightly lower at 191 mAh g^{-1}. By comparison, an a-Nb$_2$O$_5$ electrode at the rate of 1,000 mA g^{-1} showed a considerably lower capacity (73 mAh g^{-1}). The a-Nb$_2$O$_5$ electrode retained only 43% of its low-rate capacity, while the RS-Nb$_2$O$_5$ was able to retain over 70% of its low-rate capacity when discharging/charging within 12 min. When the current rate was subsequently returned to 20 mA g^{-1}, the capacity of the RS-Nb$_2$O$_5$ electrode returned to 267 mAh g^{-1}, suggesting its great reversibility and rate capability. These results are further elaborated in Supplementary Fig. 12, which highlights the dramatic difference of the two electrodes through cyclic voltammetry, dQ/dV and rate capability.

The cycle life of the RS-Nb$_2$O$_5$ and a-Nb$_2$O$_5$ electrodes at a current rate of 200 mA g^{-1} is shown in Fig. 5b. The RS-Nb$_2$O$_5$ electrode exhibited a high reversible capacity of 224 mAh g^{-1} at the 400th cycle with a 0.02% capacity loss. During the first four formation cycles of

RS-Nb$_2$O$_5$ (at 20 mA g^{-1}), the initial Coulombic efficiency was 75%. After ten cycles, the Coulombic efficiency of the electrode exceeded 99%. By the 400th cycle, the electrode demonstrated a Coulombic efficiency of more than 99.93%. By comparison, the a-Nb$_2$O$_5$ electrode exhibited a Coulombic efficiency of 98.78% and experienced a capacity loss of more than 15% by the 400th cycle. The improved stability of the RS-Nb$_2$O$_5$ electrode can be attributed to the retention of its cubic framework and its nanostructure throughout the lithiation/delithiation processes (Supplementary Fig. 13).

Charge storage and transport kinetics of RS-Nb$_2$O$_5$

To elucidate the lithium migration mechanisms in Li$_3$Nb$_2$O$_5$, we calculated the kinetically resolved activation barriers[40] for 38 Li hopping paths sampled from six representative low-energy configurations to account for the possible effect of the local environments. In contrast to the DRX lithium transition metal oxide cathodes[21,41], we find that a direct octahedral–octahedral hop is preferred compared to an octahedral–tetrahedral–octahedral hop (Supplementary Fig. 14). The local environment along the octahedral–octahedral hop can be characterized by x-Li, where $0 \leq x \leq 4$ is the number of Li ions occupying the neighbouring edge-sharing octahedral sites of a migration path (Supplementary Fig. 15). The number of Nb
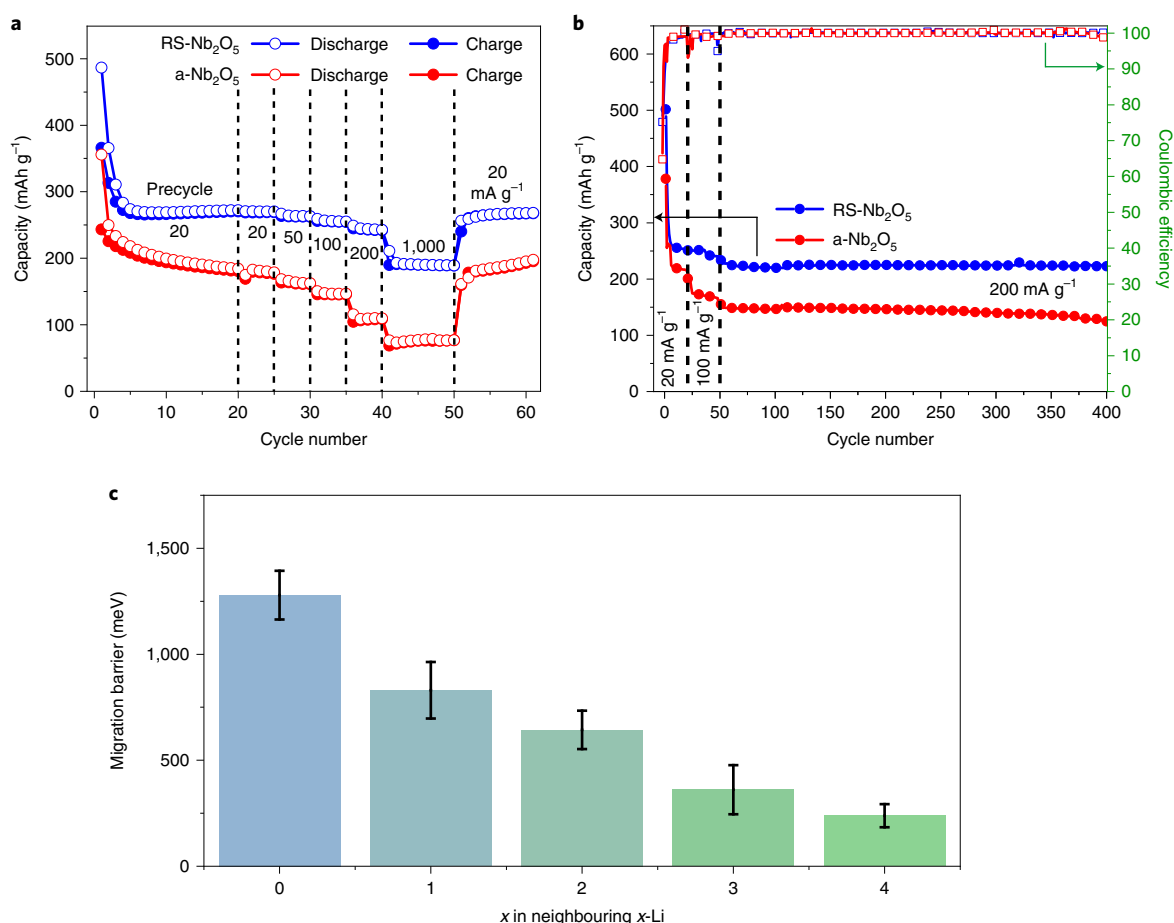
Fig. 5 | Electrochemical performance of RS-Nb$_2$O$_5$ and a-Nb$_2$O$_5$ samples with calculated migration barrier for RS-Li$_3$Nb$_2$O$_5$. a, Rate capability of RS- and a-Nb$_2$O$_5$ electrodes. While the a-Nb$_2$O$_5$ electrode retained 43% of its low-rate capacity at a 1,000 mA g^{-1} current rate, the RS-Nb$_2$O$_5$ electrode was able to retain over 70% of its low-rate capacity under the same condition. **b**, Comparison of the cycling stability of RS- and a-Nb$_2$O$_5$ electrodes. By the 400th cycle, the RS-Nb$_2$O$_5$ electrode reached a Coulombic efficiency of 99.93%, as compared to the 98.78% Coulombic efficiency of the a-Nb$_2$O$_5$ electrode. **c**, Distributions of Li migration barriers at the end of discharge in RS-Li$_3$Nb$_2$O$_5$. The different local environments are categorized by the number of neighbouring sites occupied with Li ions, and thus termed neighbours x-Li ($0 \leq x \leq 4$). There are 2, 12, 12, 10 and 2 hopping paths for 0-, 1-, 2-, 3- and 4-Li local environments, respectively. For each local environment, a distribution of calculated nudged elastic band barriers with standard deviation represented by an error bar is shown.

occupying the neighbouring sites is $4 - x$. As shown in Fig. 5c, an increase in x-Li significantly decreases the migration barriers due to lower electrostatic repulsion from Li$^+$ compared to Nb$^{3+/4+}$.

While the migration barriers for two or fewer Li in neighbouring octahedra are >750 meV, the 4-Li and 3-Li pathways have barriers below 350 meV, which are significantly lower than the 420–520 meV observed for lithium migration in graphite[42]. This observation is similar to what has been reported for DRX cathodes, where a larger number of transition metals adjacent to the intermediate tetrahedral site also leads to higher barriers[43]. Assuming a completely random arrangement of Li and Nb, we expect that 4-Li and 3-Li hops would form ~47% ($0.6^4 + {}^4C_3 \, 0.6^3 \, 0.4$) of migration pathways in Li$_3$Nb$_2$O$_5$, creating a percolating network of low-barrier pathways for fast Li diffusion.

To comprehensively investigate the charge storage and transport kinetics of RS-Nb$_2$O$_5$, we conducted kinetic analyses through GITT and cyclic voltammetry with varying scan rates[44,45], respectively (Extended Data Fig. 1 and Supplementary Fig. 16). The studies provide further evidence of the enhanced kinetics of the new cubic phase compared to its amorphous counterpart through improved ion mobility. These exceptional properties of RS-Nb$_2$O$_5$ facilitate high power performance.

Electrical properties of RS-Nb$_2$O$_5$

Intercalation electrode materials are mixed ionic and electronic conductors. The electrical conductivity of the materials has a significant impact on their power performance[46]. Therefore, the electrical conductivity of RS- Nb$_2$O$_5$ was evaluated through Mott–Schottky analysis and two-point probe conductivity measurement, as well as PF-TUNA for comparison to a-Nb$_2$O$_5$ (Fig. 6 and Supplementary Table 2). Mott–Schottky analysis (Supplementary Fig. 17) was carried out for pristine, a-Nb$_2$O$_5$ and RS-Nb$_2$O$_5$ samples (Fig. 6a). The positive slope in Fig. 6a for each sample indicates an n-type semiconductor response where electrons are the major charge carriers, as expected for Nb$_2$O$_5$ (refs. [5,6,47]). The more depressed the slope in the Mott–Schottky curves, the higher the concentration of carriers accordingly. As shown in Supplementary Table 2, RS-Nb$_2$O$_5$ exhibited the highest charge carrier concentration.

Besides the Mott–Schottky measurements, a two-point probe measurement (Supplementary Fig. 18 and Supplementary Table 2)[46,48] was carried out to determine the overall electrical conductivity of the samples. The electrical conductivity of RS-Nb$_2$O$_5$ is ×33 higher than that of a cycled a-Nb$_2$O$_5$, and over four orders of magnitude higher than the pristine amorphous Nb$_2$O$_5$. Together with the Mott–Schottky results, the increased electrical conductivity of
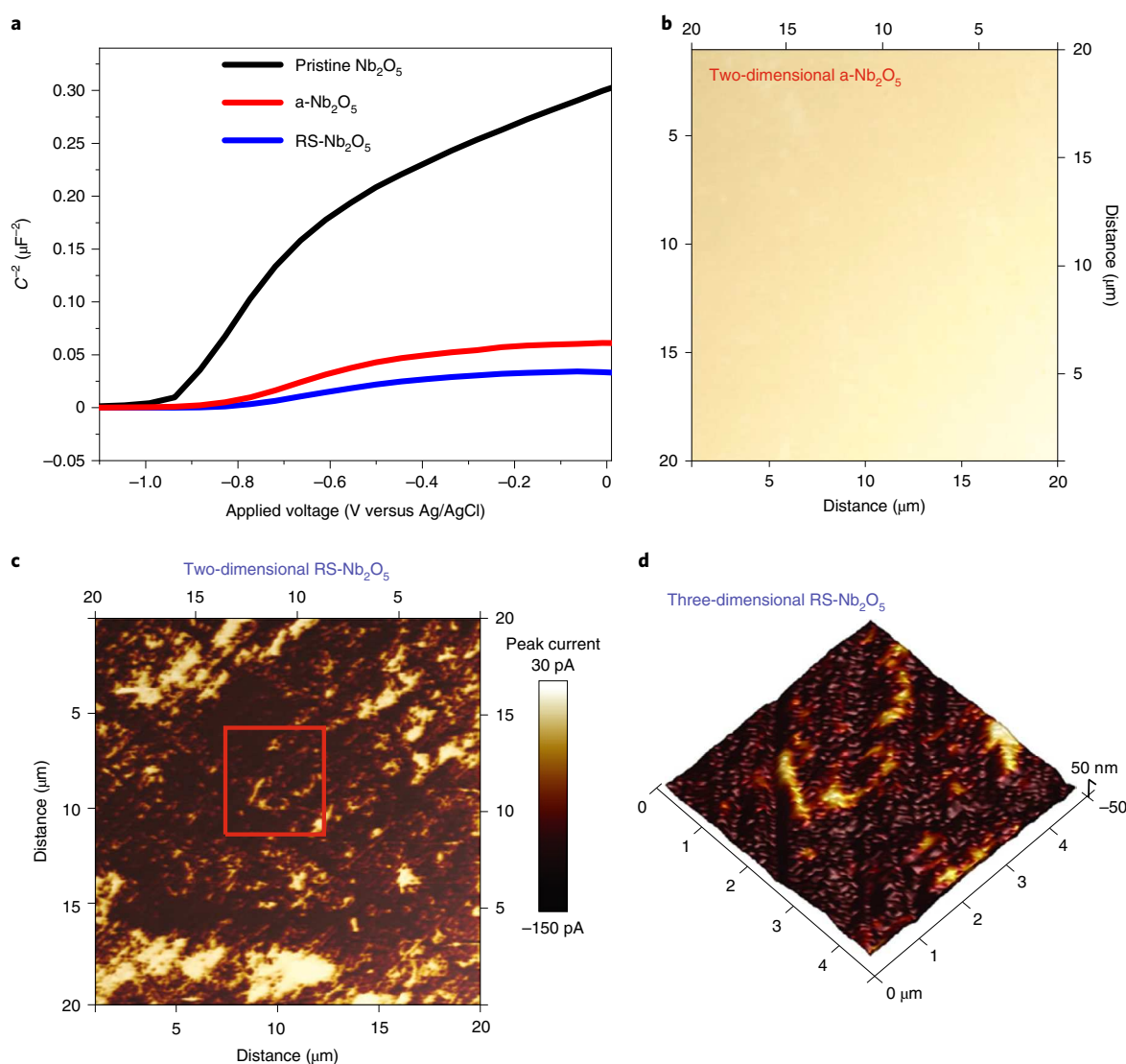
Fig. 6 | Characterization of the electrical conductivity of RS-Nb$_2$O$_5$ and a-Nb$_2$O$_5$ samples. a, Mott–Schottky analysis for pristine, a-Nb$_2$O$_5$ and RS-Nb$_2$O$_5$ samples. *C* is the space charge capacitance. The RS-Nb$_2$O$_5$ had the highest concentration of charge carriers. In addition, it showed the lowest flat-band potential, suggesting that it requires the lowest potential to reach an equivalent electron density in the bulk and interface, and thus is more conductive than its counterparts. **b,c**, PF-TUNA images of the peak current map for the cycled a- and RS-Nb$_2$O$_5$ samples, respectively. The observed average current of the RS-Nb$_2$O$_5$ sample was two orders of magnitude higher than that of the a-Nb$_2$O$_5$ sample. **d**, The overlay of a PF-TUNA current map on topography of the red boxed area in **c** of the RS-Nb$_2$O$_5$ electrode.

RS-Nb$_2$O$_5$ indicates that both charge carrier concentration and electron mobility have increased in the new RS-Nb$_2$O$_5$ structure.

PF-TUNA imaging was conducted on cycled a-Nb$_2$O$_5$ and RS-Nb$_2$O$_5$ samples (Fig. 6b–d) to simultaneously map the electrical conductivity and topography of each sample. PF-TUNA imaging of the pristine sample suggests negligible conductivity (Supplementary Fig. 19a), indicating its insulating nature. While conductance in the cycled a-Nb$_2$O$_5$ sample (Fig. 6b) increased compared to the pristine sample, the observed average current of RS-Nb$_2$O$_5$ (Fig. 6c) was two orders of magnitude higher than that of a-Nb$_2$O$_5$. The three-dimensional image in Fig. 6d features electrical current mapping overlaid on topography to provide direct visualization of the current distribution across the surface of RS-Nb$_2$O$_5$. The higher TUNA current in RS-Nb$_2$O$_5$ suggests that the a-to-c transformation has led to higher electrical conductivity, consistent with the results from the two-point probe measurements. The PF-TUNA imaging indicates that despite the greatly increased electrical conductivity of

the RS-Nb$_2$O$_5$ electrode relative to the a-Nb$_2$O$_5$ electrode, the surface was still heterogeneous at the nanoscale. Within the $5 \times 5\,\mu m^2$ region shown in Fig. 6d, uneven current distribution was observed over the surface. We postulate that the observed heterogeneity is associated with the phase transformation process, which self-adapts to promote the lowest migration barriers for both ion and electron transport.

Rock-salt formation of various ceramic materials

Previously, Xiong et al. have discovered an a-to-c transformation in a TiO$_2$ nanotube electrode during electrochemical lithiation[18]. We resolved the structure of the crystalline TiO$_2$ through Rietveld refinement as a rock-salt phase ($Fm\bar{3}m$) instead of the initial assignment of a spinel phase ($Fd\bar{3}m$; Supplementary Fig. 19a,b and Supplementary Table 3). The RS-TiO$_2$ exhibited a superior rate performance (Supplementary Fig. 19c). Mott–Schottky analysis of RS-TiO$_2$ showed that the electrode has a three-orders-of-magnitude-higher charge carrier concentration ($8.76 \times 10^{21}\,N\,cm^{-3}$) than that

$(2.01 \times 10^{19} \, \text{N cm}^{-3})$ of a typical anatase TiO_2 (ref. [46]). Based on our studies in both Nb_2O_5 and TiO_2 systems along with recent works in other metal oxide systems[18,21], we postulate that electrochemically driven crystallization in metal oxide electrodes may provide a generalizable concept in materials synthesis for electrode materials with high capacity, power and cycling stability. We underscore the importance of overcoming the nucleation barriers for the new rock-salt phase by manipulating the overpotential for the transformation during electrochemical cycling (for example, lithiation below 1.1 V for the a-to-c transformation in Nb_2O_5).

We evaluated the energy difference between the rock-salt structure and the ground-state structure for other transition metal oxides (Supplementary Fig. 21) as a metric for the likelihood of rock-salt formation. TiO_2 (ref. [18]), V_2O_5 (ref. [21]) and Nb_2O_5, which have all been demonstrated to form DRXs during electrochemical cycling, have low calculated energy differences. In general, the group VIB and VIIB transition metal oxides are less stable (larger energy differences) than group IVB and VB transition metal oxides, with the exception of Mn. In particular, Ta_2O_5 is predicted to be another potential candidate for DRX formation.

In summary, we report a rock-salt Nb_2O_5 electrode material produced through an electrochemically driven crystallization of an amorphous nanochanneled Nb_2O_5. The RS-Nb_2O_5 exhibits multi-electron redox per Nb for Li-ion storage. DFT calculations reveal significant low-energy lithium migration paths that lead to the exceptional electrochemical performance of the RS-Nb_2O_5. The cubic structure affords a material with high rate performance due to increased Li-ion diffusivity and electrical conductivity. In parallel, the crystal displays high stability owing to the structural integrity upon lithiation/delithiation. The self-organization of atoms into the optimal crystalline structure during electrochemical cycling suggests a synthetic avenue to access rare metal oxide structures with unique properties. The utilization of electrochemical cycling to form novel crystalline structures can be advantageous in designing other enhanced electrode materials.

Online content

Any methods, additional references, Nature Research reporting summaries, source data, extended data, supplementary information, acknowledgements, peer review information; details of author contributions and competing interests; and statements of data and code availability are available at https://doi.org/10.1038/s41563-022-01242-0.

References

1. Melot, B. C. & Tarascon, J. M. Design and preparation of materials for advanced electrochemical storage. *Acc. Chem. Res.* **46**, 1226–1238 (2013).
2. Ohzuku, T., Sawai, K. & Hirai, T. Electrochemistry of L-niobium pentoxide in a lithium/non-aqueous cell. *J. Power Sources* **19**, 287–299 (1987).
3. Reichman, B. & Bard, A. J. The application of Nb_2O_5 as a cathode in non-aqueous lithium cells. *J. Electrochem. Soc.* **128**, 344–346 (1981).
4. Nowak, I. & Ziolek, M. Niobium compounds: preparation, characterization, and application in heterogeneous catalysis. *Chem. Rev.* **99**, 3603–3624 (1999).
5. Aegerter, M. A. Sol–gel niobium pentoxide: a promising material for electrochromic coatings, batteries, nanocrystalline solar cells and catalysis. *Sol. Energy Mater. Sol. Cells* **68**, 401–422 (2001).
6. Le Viet, A., Reddy, M. V., Jose, R., Chowdari, B. V. R. & Ramakrishna, S. Nanostructured Nb_2O_5 polymorphs by electrospinning for rechargeable lithium batteries. *J. Phys. Chem. C* **114**, 664–671 (2010).
7. Kim, J. W., Augustyn, V. & Dunn, B. The effect of crystallinity on the rapid pseudocapacitive response of Nb_2O_5. *Adv. Energy Mater.* **2**, 141–148 (2012).
8. Yan, L. T. et al. Recent advances in nanostructured Nb-based oxides for electrochemical energy storage. *Nanoscale* **8**, 8443–8465 (2016).
9. Brezesinski, K. et al. Pseudocapacitive contributions to charge storage in highly ordered mesoporous group V transition metal oxides with iso-oriented layered nanocrystalline domains. *J. Am. Chem. Soc.* **132**, 6982–6990 (2010).
10. Augustyn, V. et al. High-rate electrochemical energy storage through Li+ intercalation pseudocapacitance. *Nat. Mater.* **12**, 518–522 (2013).
11. Wang, X. L. et al. High-performance supercapacitors based on nanocomposites of Nb_2O_5 nanocrystals and carbon nanotubes. *Adv. Energy Mater.* **1**, 1089–1093 (2011).
12. Mukherjee, R., Krishnan, R., Lu, T. M. & Koratkar, N. Nanostructured electrodes for high-power lithium ion batteries. *Nano Energy* **1**, 518–533 (2012).
13. Wei, M. D., Qi, Z. M., Ichihara, M. & Zhou, H. S. Synthesis of single-crystal niobium pentoxide nanobelts. *Acta Materialia* **56**, 2488–2494 (2008).
14. Brauer, G. Die oxyde des niobs. *Z. Anorg. Allg. Chem.* **248**, 1–31 (1941).
15. Schäfer, H., Gruehn, R. & Schulte, F. The modifications of niobium pentoxide. *Angew. Chem. Int. Ed.* **5**, 40–52 (1966).
16. Griffith, K. J., Forse, A. C., Griffin, J. M. & Grey, C. P. High-rate intercalation without nanostructuring in metastable Nb_2O_5 bronze phases. *J. Am. Chem. Soc.* **138**, 8888–8899 (2016).
17. Pralong, V. Lithium intercalation into transition metal oxides: a route to generate new ordered rock salt type structure. *Prog. Solid State Chem.* **37**, 262–277 (2009).
18. Xiong, H. et al. Self-improving anode for lithium-ion batteries based on amorphous to cubic phase transition in TiO_2 nanotubes. *J. Phys. Chem. C* **116**, 3181–3187 (2012).
19. Yildirim, H., Greeley, J. P. & Sankaranarayanan, S. K. R. S. Concentration-dependent ordering of lithiated amorphous TiO_2. *J. Phys. Chem. C* **117**, 3834–3845 (2013).
20. Jung, H. et al. Redox cycling driven transformation of layered manganese oxides to tunnel structures. *J. Am. Chem. Soc.* **142**, 2506–2513 (2020).
21. Liu, H. D. et al. A disordered rock salt anode for fast-charging lithium-ion batteries. *Nature* **585**, 63–67 (2020).
22. Schmuki, P. & Virtanen, S. (eds) *Electrochemistry at the Nanoscale* (Springer, 2009).
23. Liu, C. F., Neale, Z. G. & Cao, G. Z. Understanding electrochemical potentials of cathode materials in rechargeable batteries. *Mater. Today* **19**, 109–123 (2016).
24. Sasaki, T., Ukyo, Y. & Novak, P. Memory effect in a lithium-ion battery. *Nat. Mater.* **12**, 569–575 (2013).
25. Madej, E., La Mantia, F., Schuhmann, W. & Ventosa, E. Impact of the specific surface area on the memory effect in Li-ion batteries: the case of anatase TiO_2. *Adv. Energy Mater.* https://doi.org/10.1002/aenm.201400829 (2014).
26. Ventosa, E., Loffler, T., La Mantia, F. & Schuhmann, W. Understanding memory effects in Li-ion batteries: evidence of a kinetic origin in TiO_2 upon hydrogen annealing. *Chem. Commun.* **52**, 11524–11526 (2016).
27. Ovejas, V. J. & Cuadras, A. Effects of cycling on lithium-ion battery hysteresis and overvoltage. *Sci. Rep.* https://doi.org/10.1038/s41598-019-51474-5 (2019).
28. Dahlman, C. J. et al. Dynamics of lithium insertion in electrochromic titanium dioxide nanocrystal ensembles. *J. Am. Chem. Soc.* **143**, 8278–8294 (2021).
29. Scherrer, P. The space grid of aluminium. *Phys. Z.* **19**, 23–27 (1918).
30. Garbassi, F., Bart, J. C. J. & Petrini, G. XPS study of tellurium—niobium and tellurium—tantalum oxide systems. *J. Electron Spectrosc. Relat. Phenom.* **22**, 95–107 (1981).
31. Ozer, N., Rubin, M. D. & Lampert, C. M. Optical and electrochemical characteristics of niobium oxide films prepared by sol-gel process and magnetron sputtering. A comparison. *Sol. Energy Mater. Sol. Cells* **40**, 285–296 (1996).
32. Bahl, M. K. ESCA studies of some niobium compounds. *J. Phys. Chem. Solids* **36**, 485–491 (1975).
33. Simon, D., Perrin, C. & Baillif, P. Electron spectrometry study (ESCA) of niobium and its oxides. Application to the oxidation at high temperature and low oxygen pressure. *C. R. Hebd. Acad. Sci. Ser. C* **283**, 241–244 (1976).
34. Jouve, J., Belkacem, Y. & Severac, C. X-ray photoelectron-spectroscopy study of phosphorus incorporation in anodic oxide-films on niobium. *Thin Solid Films* **139**, 67–75 (1986).
35. Verma, P., Maire, P. & Novak, P. A review of the features and analyses of the solid electrolyte interphase in Li-ion batteries. *Electrochim. Acta* **55**, 6332–6341 (2010).
36. Monfort, Y., Maisseu, A., Allais, G., Deschanv, A. & Delavign, P. Structure and morphology of niobium suboxides. *Phys. Status Solidi A Appl. Res.* **15**, 129–142 (1973).
37. Yabuuchi, N. et al. High-capacity electrode materials for rechargeable lithium batteries: Li_3NbO_4-based system with cation-disordered rocksalt structure. *Proc. Natl Acad. Sci. USA* **112**, 7650–7655 (2015).
38. Preefer, M. B. et al. Multielectron redox and insulator-to-metal transition upon lithium insertion in the fast-charging, Wadsley-Roth phase PNb_9O_{25}. *Chem. Mater.* **32**, 4553–4563 (2020).
39. Griffith, K. J., Wiaderek, K. M., Cibin, G., Marbella, L. E. & Grey, C. P. Niobium tungsten oxides for high-rate lithium-ion energy storage. *Nature* **559**, 556–563 (2018).
40. Van der Ven, A., Ceder, G., Asta, M. & Tepesch, P. D. First-principles theory of ionic diffusion with nondilute carriers. *Phys. Rev. B* https://doi.org/10.1103/PhysRevB.64.184307 (2001).

41. Lee, J. et al. Unlocking the potential of cation-disordered oxides for rechargeable lithium batteries. *Science* **343**, 519–522 (2014).

42. Thinius, S., Islam, M. M., Heitjans, P. & Bredow, T. Theoretical study of Li migration in lithium-graphite intercalation compounds with dispersion-corrected DFT methods. *J. Phys. Chem. C* **118**, 2273–2280 (2014).

43. Acevedo-Pena, P. & Gonzalez, I. EIS characterization of the barrier layer formed over Ti during its potentiostatic anodization in 0.1 M HClO$_4$/x mM HF (1 mM ≤ x ≤ 500 mM). *J. Electrochem. Soc.* **159**, C101–C108 (2012).

44. Conway, B. E., Birss, V. & Wojtowicz, J. The role and utilization of pseudocapacitance for energy storage by supercapacitors. *J. Power Sources* **66**, 1–14 (1997).

45. Wang, J., Polleux, J., Lim, J. & Dunn, B. Pseudocapacitive contributions to electrochemical energy storage in TiO$_2$ (anatase) nanoparticles. *J. Phys. Chem. C* **111**, 14925–14931 (2007).

46. Savva, A. I. et al. Defect generation in TiO$_2$ nanotube anodes *via* heat treatment in various atmospheres for lithium- ion batteries. *Phys. Chem. Chem. Phys.* **20**, 22537–22546 (2018).

47. Rani, R. A., Zoolfakar, A. S., O'Mullane, A. P., Austin, M. W. & Kalantar-Zadeh, K. Thin films and nanostructures of niobium pentoxide: fundamental properties, synthesis methods and applications. *J. Mater. Chem. A* **2**, 15683–15703 (2014).

48. Islam, S. Z., Reed, A., Wanninayake, N., Kim, D. Y. & Rankin, S. E. Remarkable enhancement of photocatalytic water oxidation in N$_2$/Ar plasma treated, mesoporous TiO$_2$ films. *J. Phys. Chem. C* **120**, 14069–14081 (2016).

Methods

Electropolishing of Nb metal. The NCNO samples were prepared based on a method reported previously[49]. In short, Nb foil of 127 μm thickness (35×40 mm^2, Alfa Aesar, 99.8% annealed) was cut; sonicated sequentially in acetone, isopropanol and deionized water for 5 min each; and electropolished in 2 M sulfuric acid (Fisher Scientific, 95–98%) in methanol (Fisher Scientific, 99.9%) solution. Electropolishing was conducted at 15 V with a Pt mesh counter electrode at –70 °C for 2 hours.

NCNO synthesis. NCNOs were prepared by electrochemical anodization of Nb metal, using a method adopted from work by Schmuki et al.[50]. Using 10 wt% K$_2$HPO$_4$ in glycerol solution at 180 °C, the Nb film was anodized at 25 V from 5 min up to 15 min. The as-anodized samples were then ultrasonically cleaned in deionized water for 2 min. NCNO samples were then placed under vacuum and dried overnight at 110 °C. The NCNO electrode contains a high density of channels (4×10^{14} pores m^{-2}), resulting in a surface area of 60–80 m^2 g^{-1} (via SEM image analysis). This agrees with results from anodized aluminium oxides with similar pore structures[51].

TiO$_2$ nanotube synthesis. Ti foil (Alfa Aesar, 32 μm thick) was cut into 4 cm × 4.5 cm pieces and sonicated in acetone, isopropanol and deionized water for 5 minutes each. The prepared foil was then anodized in a solution of 0.27 M NH$_4$F in formamide (Fisher Scientific), with Pt mesh as the counter electrode, for 30 minutes at 15 V. The as-anodized samples were then ultrasonically cleaned in nanopure water. Samples were dried overnight in a vacuum oven at 110 °C.

Structural characterizations. Grazing-incidence synchrotron X-ray diffraction measurements were conducted at Sector 12-ID-D, Advanced Photon Source at Argonne National Laboratory. The X-ray wavelengths of both $\lambda = 0.684994$ Å and 0.61990 Å were used in this study. For varying the structural probing depths, a series of incidence angles (α) from 0° up to 1° were adopted in the grazing-incidence synchrotron X-ray diffraction measurements. In order to minimize the scattering contribution from the bulk Nb foil substrate, we placed the sample on top of a convex Teflon support for the measurements where the tail of the incident X-ray beam sweeps through the surface layer of the electrode samples. Additional in-house X-ray diffraction measurements were taken with a Rigaku Miniflex diffractometer with Cu Kα irradiation at $\lambda = 1.5406$ Å. XPS samples were loaded without air exposure through an Ar glove box connected directly to the ultra-high vacuum system. XPS measurements were performed using a Specs PHOIBOS 150 hemispherical energy analyser with a monochromated Al Kα X-ray source. Survey and core level spectra were collected using a pass energy of 40 and 20 eV, respectively, and all spectra were referenced to the binding energy of sp^3-hybridized carbon at 284.8 eV. XAS at beamline 12-BM-B at Argonne National Laboratory was used to determine the chemical environment of the materials. Samples for XAS were prepared with free-standing NCNO films peeled off from a Nb substrate. The films were placed onto a copper current collector and cycled in a Li half-cell. SEM images were taken with an FEI Teneo field emission SEM instrument. SEM images were analysed using the National Institutes of Health ImageJ v.1.8 to determine pore size, size distribution and surface area of the oxides. TEM, high-resolution TEM and SAED characterizations of the samples were completed on a JEOL JEM-2100 at an acceleration voltage of 200 kV. TEM characterizations were also completed on a JEOL JEM2100F microscope with a working voltage of 200 kV. A Zeiss NVision 40 was employed to prepare a TEM specimen (RS-Nb$_2$O$_5$ electrode after 100 cycles). By following the standard focused ion beam lift-out procedure, the lamella was transferred to a TEM grid. A 30 kV Ga beam was employed for general milling. The final lamella was showered by a 5 kV Ga beam to reduce the ion beam damage from the 30 kV Ga beam.

Inductively coupled plasma mass spectrometry was conducted on a Thermo Fisher iCAP RQ ICP-MS coupled to a Teledyne Analyte Excite+ 193 nm laser ablation system. Each sample measurement is an average of three replicate analyses, each consisting of a gas-blank-subtracted ablation peak, and each of which are the average of 100 sweeps over 5 s. Elemental concentrations are standardized against standard glasses (GSD and GSE*), except P, Ge and Se, which were standardized against sequential dilutions of single-element inductively coupled plasma mass spectrometry standards. Concentrations are reported in the form of grams of analyte per gram sample ×100 (wt%) assuming a sample volume for samples and standards. No detection indicates samples that had a reading below the limit of detection, which is defined as three times the background measured before each ablation pass. GSE was measured at the largest possible spot size to compare accuracy at count rates comparable to that of the unknowns. Accepted values are from the GeoReM database preferred values (mean of new analyses).

Time-of-flight secondary-ion mass spectrometry measurement was performed at Environmental Molecular Sciences Laboratory, which is located at Pacific Northwest National Laboratory. A TOF.SIMS5 instrument (IONTOF) was used. Dual beam depth profiling was used. A 2.0 keV Cs$^+$ beam was used as the sputtering beam, and a 25 keV Bi$^+$ beam was used as the analysis beam for signal collection. The Cs$^+$ sputtering beam (~65 nA) was scanned over a 200×200 μm^2 area, and the equivalent sputter rate (SiO$_2$ as a reference) was about 0.75 nm s^{-1}. The Bi$^+$ beam was focused to be about 5 μm in diameter with a beam current that was

about 0.70 pA with a 10 kHz frequency. The Bi$^+$ beam was scanned over an area of 70×70 μm^2 at the Cs$^+$ sputter crater centre. A low-energy (10 eV) electron flood gun was used for charge compensation in all measurements.

Electrochemical characterizations. Working electrodes were cut into 15-mm-diameter discs using a disc cutter (EQ-T06-Disc, MTI, Corporation). All batteries were prepared in an argon-filled glove box (MBraun) where oxygen levels were maintained below 0.5 ppm. Electrodes removed from cells for analysis were thoroughly washed with dry dimethyl carbonate (Aldrich) and allowed to dry under the inert atmosphere. Li half-cells were assembled in coin-type cells (Hohsen 2032) with Li metal foil (FMC) as the counter electrode, microporous polyolefin separators (Celgard 2325) and 1.2 M LiPF$_6$ in ethylene-carbonate/ethyl-methyl-carbonate (3:7 weight ratio) electrolyte (Gen II, Tomiyama). Half-cells were cycled galvanostatically between 3 and 0.5 V versus Li/Li$^+$ using an automated Maccor battery tester at 25 °C. Four cells were electrochemically tested to confirm reproducibility (Supplementary Fig. 22). A three-electrode cell ECC-ref (EL-Cell) was used for the GITT measurements. The cell was made with Li metals as both the reference electrode and the counter electrode, glassy fibre separators (Whatman 2325) and Gen II electrolyte. The current was applied at 60 μA for 30 min, which was followed by a 12 h relaxation to approach the steady state, where the voltage variation is <2 mV h^{-1}.

The mass of the Nb$_2$O$_5$ films was determined by dissolution of the oxide film in 1% HF in concentrated HCl solution and by measuring the weight difference of the samples before and after etching. This solution allows selective etching of Nb$_2$O$_5$ over Nb. The remaining substrate was examined by SEM and energy-dispersive X-ray spectroscopy at 5 kV using an FEI Teneo field emission SEM instrument to ensure that no residual Nb$_2$O$_5$ was left on the substrate. The mass loading of the electrodes was determined to be ~1.06 ± 0.25 mg cm^{-2}.

Two-point probe measurements, Mott–Schottky analysis and PF-TUNA. Two-point electrical conductivity measurements and PF-TUNA were used to determine the out-of-plane (that is, through-sample) conductivity of NCNO. For the two-point probe measurements, a silver paint contact was placed on the surface of the oxide film with another point of contact to the Nb foil. The contacts were then connected to the measurement device set-up with Au wires. A current ranging from 0.2 to 20 μA was applied by a Keithley 237 High Voltage Source Measurement Unit, and the resulting voltage was recorded by a Keithley 2000 Multimeter.

Mott–Schottky analysis was performed using the SPEIS program on a Bio-Logic VMP-240 in a three-electrode cell (EL-Cell). Kapton tape was used as a mask, leaving a disc electrode of 12.7 mm diameter for the niobium oxide sample. A Pt mesh counter electrode and a Ag/AgCl reference electrode were used in an aqueous 1 M NaOH solution for Nb$_2$O$_5$ samples or 1 M KOH for TiO$_2$ samples. The charge carrier concentration of the samples was determined by the space charge capacitance (C_{sc})[52] obtained from the imaginary part of the impedance Z'':

$$C_{sc} = -\frac{1}{2\pi f Z''} \tag{1}$$

where f is the frequency. Bode plots in the frequency range of 100 mHz to 100 kHz with a voltage amplitude of 10 mV from 0.1 to −1 V versus Ag/AgCl in 0.05 V increments were collected to determine the frequency at which the impedance $|Z|$ is constant for all samples and is suitable for Mott–Schottky analysis, as seen in Supplementary Fig. 17.

The $|Z|$ plateaus at a frequency of about 1 kHz; therefore, the curves at 1.486 kHz were used to calculate the charge carrier density for each sample. The flat-band potential can also be obtained from the Mott–Schottky plots by finding the x intercept of the tangent line to the linear region of each curve. The following equation relates the charge carrier density to the capacitance of the sample, where q is the charge of an electron, ε is the dielectric constant (assumed to be a constant value of 42), ε_0 is the vacuum permittivity constant, N_D is the charge carrier density, A is the geometric surface area, V_{fb} is the flat-band potential, V is the applied potential, k is Boltzmann's constant and T is the absolute temperature in Kelvin[52].

$$C_{sc}^{-2} = \left(\frac{2}{q\varepsilon\varepsilon_0 N_D A^2} \right) \left(V - V_{fb} - \frac{kT}{q} \right) \tag{2}$$

Equation 2 is then differentiated with respect to the voltage to obtain the charge carrier density, as shown in equation (3).

$$N_D = \frac{2}{q\varepsilon\varepsilon_0 A^2} \left(\frac{dC^{-2}}{dV} \right)^{-1} \tag{3}$$

Ex situ PF-TUNA was performed using a Bruker Dimension Icon atomic force microscope in an Ar-filled MBraun glove box with <0.1 ppm water and oxygen. PF-TUNA provides spatially resolved nanoscale through-sample conductivity maps of resistive materials in response to an applied bias. A Bruker DDESP conductive diamond tip probe (100 nm nominal radius of curvature tip composed of 0.01–0.025 Ω cm antimony-doped (n-doped) Si) with a set-point force of 70 nN was used to simultaneously image the electrode topography and conductivity. The electrodes were placed directly onto the metallic vacuum chuck, and a bias

voltage of −10 V was applied to the chuck (that is, bottom surface of the electrode). Then $20 \times 20\,\mu m^2$ images were acquired at a TUNA gain sensitivity of 20 pA V^{-1} (±10 V full scale, corresponding to ±200 pA sensitivity) with $1,024 \times 1,024$ pixels (i.e., ~20 nm x 20 nm square pixels, although the actual lateral resolution is a more complicated function of probe contact area and effective sampling volume) to generate high resolution current maps. Images were processed and analysed in Nanoscope Analysis version 1.90. A first-order plane fit was applied to the raw topographical data to account for sample tip and tilt, with an additional first-order flatten applied to correct for small line-to-line offsets in the piezo for Z direction. A conductivity skin was then overlaid on the three-dimensional topography image to visualize variations in current density via colour contrast.

DFT calculations. All DFT calculations were carried out using the Vienna Ab initio Simulation Package[53] within the projector augmented-wave approach[54]. The Perdew–Burke–Ernzerhof generalized gradient approximation[55] was adopted for the exchange–correlation functional. The kinetic energy cut-off was set to 520 eV, and a k-point density of at least 1,000 per reciprocal atom was used for structural relaxations of Nb_2O_5. The electronic energy and atomic forces were converged to within 10^{-5} eV and 0.02 eV Å^{-1}, respectively, in line with the settings in the Materials Project database[56].

Structure enumeration. First, we enumerated and calculated the energies of all orderings in a $\sqrt{5} \times \sqrt{5} \times 2$ supercell of cubic rock-salt $Li_3Nb_2O_5$. The Li and Nb occupancy of the octahedral sites (Wyckoff symbol, 4b) in a face-centred cubic oxygen lattice was set at x-Li/0.4-Nb, where x ranges from 0 to 0.6 in increments of 0.1. Lithium was then removed in 0.5 increments from $Li_3Nb_2O_5$, and the symmetrically distinct orderings were then calculated for each composition. All symmetrically distinct orderings were generated with an enumeration algorithm interfaced with the Python Materials Geomics (pymatgen) library[57,58]. These orderings were then fully relaxed using DFT calculations, and the lowest energy configurations were used for subsequent analysis.

Intercalation voltage profile. The pseudo-binary stability diagrams for $Li_xNb_2O_5$ ($0 \le x \le 3$) were constructed from previous structure enumeration and DFT relaxations. The stable intermediate phases in the stability diagram were used for static calculations with a denser Γ-centred k mesh of $9 \times 8 \times 7$ to obtain more accurate energies. The voltage profile was then obtained by computing the average voltage between any two stable intermediate phases: where E is the total DFT energy and e is the electronic charge[59].

$$V = -\frac{E\left(Li_{x_1}Nb_2O_5\right) - E\left(Li_{x_2}Nb_2O_5\right) - (x_1 - x_2)E(Li)}{(x_1 - x_2)e} \quad (4)$$

Nudged elastic band calculations. The migration barriers were calculated using climbing image nudged elastic band methods. The calculations were performed on $2\sqrt{5} \times 2\sqrt{5} \times 4$ supercells of the rock-salt primitive cell. These configurations were directly obtained by doubling each lattice vector of the low-energy structures from previous voltage profile calculations. The number of images used for all climbing image nudged elastic band calculations was five. The energies and forces were converged to 5×10^{-5} eV per supercell and 0.05 eV Å^{-1}, respectively. It is expected that the neighbouring atoms around the migration paths would have substantial effects on the barriers. In particular, there are four octahedral neighbouring atoms sharing edges with the two octahedral migrating Li atoms, and these neighbouring atoms can be occupied by either Nb or Li. Herein, six representative low-energy configurations were used as starting structures to construct the Li migration paths with x-Li and 4x-Nb occupying the edge-sharing neighbouring atoms (Fig. 5c). The barrier variation for each x is marginal, justifying the use of these representative configurations.

Data availability
The data that support the findings of this study are available from the corresponding authors on reasonable request.

References
49. Barnes, P. et al. Electropolishing valve metals with a sulfuric acid-methanol electrolyte at low temperature. *Surf. Coat. Technol.* **347**, 150–156 (2018).
50. Lee, K., Yang, Y., Yang, M. & Schmuki, P. Formation of highly ordered nanochannel Nb oxide by self-organizing anodization. *Chem. Eur. J.* **18**, 9521–9524 (2012).
51. Roslyakov, I. V. et al. Annealing induced structural and phase transitions in anodic aluminum oxide prepared in oxalic acid electrolyte. *Surf. Coat. Technol.* https://doi.org/10.1016/j.surfcoat.2019.125159 (2020).
52. Baram, N. & Ein-Eli, Y. Electrochemical impedance spectroscopy of porous TiO_2 for photocatalytic applications. *J. Phys. Chem. C* **114**, 9781–9790 (2010).
53. Kresse, G. & Furthmuller, J. Efficient iterative schemes for *ab initio* total-energy calculations using a plane-wave basis set. *Phys. Rev. B* **54**, 11169–11186 (1996).
54. Blochl, P. E. Projector augmented-wave method. *Phys. Rev. B* **50**, 17953–17979 (1994).
55. Perdew, J. P., Burke, K. & Ernzerhof, M. Generalized gradient approximation made simple. *Phys. Rev. Lett.* **77**, 3865–3868 (1996).
56. Jain, A. et al. Commentary: the materials project: a materials genome approach to accelerating materials innovation. *Appl. Mater.* https://doi.org/10.1063/1.4812323 (2013).
57. Hart, G. L. W. & Forcade, R. W. Algorithm for generating derivative structures. *Phys. Rev. B* https://doi.org/10.1103/Physrevb.77.224115 (2008).
58. Ong, S. P. et al. Python Materials Genomics (pymatgen): a robust, open-source python library for materials analysis. *Comput. Mater. Sci.* **68**, 314–319 (2013).
59. Aydinol, M. K., Kohan, A. F., Ceder, G., Cho, K. & Joannopoulos, J. *Ab initio* study of lithium intercalation in metal oxides and metal dichalcogenides. *Phys. Rev. B* **56**, 1354–1365 (1997).

Author contributions
H.X. and P.B. conceived and designed all experiments. S.P.O., Y. Zuo, J.Q., Zhuoying Zhu and C.C. designed all computational modelling work. P.B. and K.D. synthesized the materials. P.B. conducted all electrochemical measurements. S.L., P.B. and C.D. conducted structural characterization by XAS. H. Zhou, Z.M., P.B., C.D. and E.G. conducted structural characterization by synchrotron X-ray diffraction. J.G.C. and Y.D. collected XPS data. D.H., Y.L., K.S. and P.B. collected focused ion beam TEM, high-resolution TEM and SAED data. P.B., H. Zhu, O.O.M. and P.H.D. designed and performed the PF-TUNA experiments. P.B., A. B. and P.J.S. designed and collected the two-point probe measurements. Zihua Zhu, Y. Zhou and Y.D. conducted the time-of-flight secondary-ion mass spectrometry measurements. D.S. and P.B. conducted and analysed the inductively coupled plasma mass spectrometry measurements. P.B., H.X., S.L., J.G.C., D.H., H. Zhou, Z.M., P.H.D., Zihua Zhu, Y.D. and P.J.S. analysed the collected data. P.B., Y. Zuo, H.X. and S.P.O. wrote the manuscript. All authors were involved in editing the manuscript.

Competing interests
The authors declare no competing interests.

Additional information
Extended data is available for this paper at https://doi.org/10.1038/s41563-022-01242-0.

Supplementary information The online version contains supplementary material available at https://doi.org/10.1038/s41563-022-01242-0.

Correspondence and requests for materials should be addressed to Shyue Ping Ong or Hui Xiong.

Peer review information *Nature Materials* thanks the anonymous reviewers for their contribution to the peer review of this work.

Reprints and permissions information is available at www.nature.com/reprints.
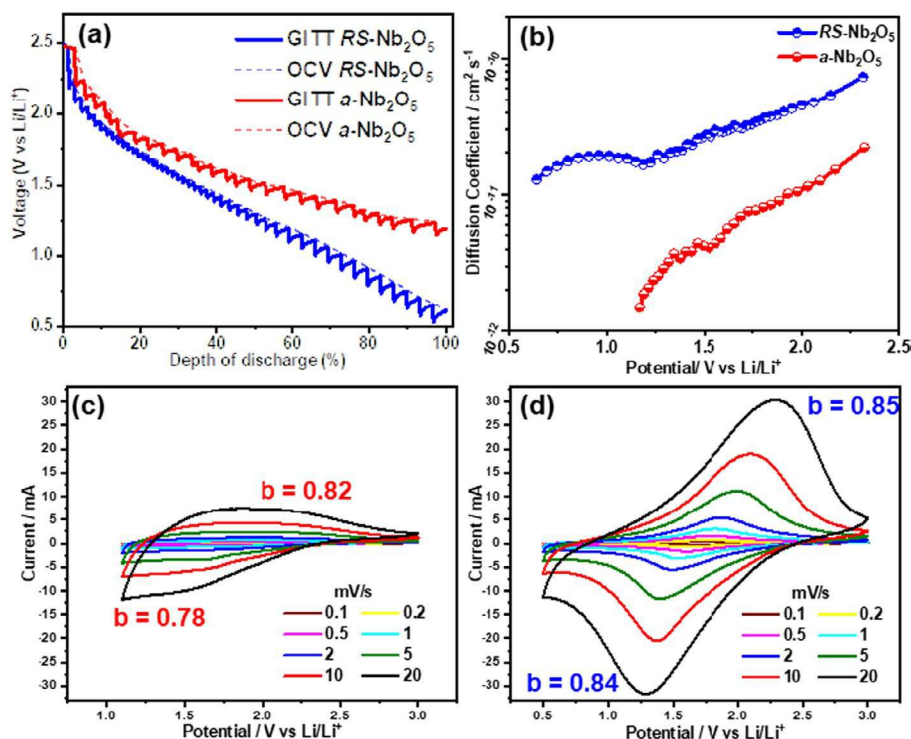
Extended Data Fig. 1 | Characterization of lithium ion diffusivity and charge storage of *RS*-Nb$_2$O$_5$ and *a*-Nb$_2$O$_5$ sample. a, GITT measurements of the *RS*- and *a*-Nb$_2$O$_5$ electrodes. **b**, The logarithmic plot of Li ion diffusivity as a function of voltage by GITT measurements. Overall, *RS*-Nb$_2$O$_5$ exhibited an order of magnitude higher Li ion diffusivity compared to *a*-Nb$_2$O$_5$ within the potential window during lithiation. During the cathodic scan, both samples experienced a gradual decrease in diffusivity as more Li$^+$ occupied the vacant sites in the host material. It is worth noting that below 1.1 V, Li$^+$ diffusivity in *RS*-Nb$_2$O$_5$ slightly increased, concurrent with the ongoing phase transformation upon cycling. Li$^+$ diffusivity in *RS*-Nb$_2$O$_5$ is also higher than that of other polymorphs of Nb$_2$O$_5$ electrodes. **c** and **d**, cyclic voltammograms of *RS*- and *a*-Nb$_2$O$_5$ electrodes at varying scan rates. Insights in terms of diffusion and capacitive contribution to Li storage can be obtained by analyzing the peak current (*i*) dependence on scan rate (*v*). For a redox reaction limited by semi-infinite diffusion, the peak current is proportional to the square root of the scan rate ($v^{1/2}$); while for a capacitive process it varies linearly with v[44,45]. A *b* value can be obtained by analyzing the power law relationship between *i* and *v* via $i = av^b$, where *a* and *b* are adjustable parameters. It was found that the *b* values for *RS*-Nb$_2$O$_5$ and *a*-Nb$_2$O$_5$ sample were ~0.85 and ~0.80, respectively. The results suggest both electrodes have mixed contribution from diffusion and capacitive process with *RS*-Nb$_2$O$_5$ electrode having a slightly higher capacitive contribution indicative of a faster kinetic in *RS*-Nb$_2$O$_5$.